ACS Catalysis

pubs.acs.org/acscatalysis Research Article

In Situ Characterization Reveals a Favorable Reconstruction of $BiVO_4$ in Thermal catalysis

Cheng Chen,[#] Yifan Xu,[#] Chunyan Ma,[#] Bolei Chen, Fanglan Geng, Xiaozhi Liu,[*] Maoyong Song,[*] and Guibin Jiang

Cite This: *ACS Catal.* 2025, 15, 15387−15394 Read Online

ACCESS | Metrics & More | Article Recommendations | Supporting Information

ABSTRACT: Reconstruction of catalysts, widely acknowledged in electrocatalysis, has rarely been explored in thermal catalysis. This study demonstrates a dynamic favorable reconstruction of $BiVO_4$ in thermal selective oxidation of benzylic C−H of toluene using *in situ* techniques. $BiVO_4$ undergoes reconstruction during high-temperature H_2 reduction, wherein Bi dissolves and aggregates into metallic Bi particle to form $Bi/BiVO_4$. $Bi/BiVO_4$ undergoes secondary reconstruction through high-temperature O_2 oxidation in thermal catalysis, wherein Bi migrates toward metallic Bi particle to form $Bi_2O_3/BiVO_4$. $Bi_2O_3/BiVO_4$ exhibits good adsorption performance on toluene and O_2, and promotes charge transport to generate more abundant active species. Therefore, a toluene conversion of 26,300.00 $\mu mol \cdot g_{cat}^{-1} \cdot h^{-1}$ and product yield of 410.00 $mmol \cdot g_{cat}^{-1}$ were achieved, giving the highest reported product yield for thermal selective oxidation of the benzylic C−H bond of toluene. Based on this, $Bi_2O_3/BiVO_4$ catalysts with high-performance can be synthesized by a one-step hydrothermal method, opening up new avenues for thermal catalyst design.

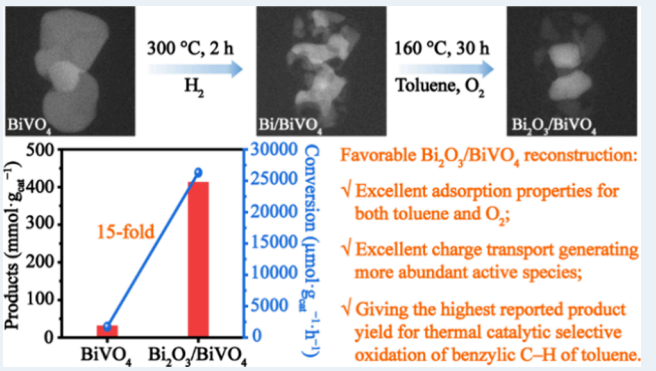

KEYWORDS: *favorable reconstruction in thermal catalysis, $Bi_2O_3/BiVO_4$ active interface, excellent adsorption performance, efficient charge transport, selective oxidation of benzylic C−H*

1. INTRODUCTION

Reconstruction of catalysts has gained widespread attention in electrocatalysis.[1−3] Importantly, this reconstruction is usually favorable and has gradually been developed into an approach to improve electrocatalytic performance.[4,5] For example, $IrNi_x$ nanoparticles undergo *in situ* reconstruction in the oxygen evolution reaction (OER).[6] Under acidic conditions, Ni dissolves, migrates, and dopes to form a Ni-doped iridium skin framework catalyst. Under alkaline conditions, Ni migrates from the bulk phase to form a NiO_x surface layer. Such self-reconstruction significantly enhances the performance of the OER in both acidic and alkaline electrolytes. Similarly, vanadium dissolves to create a β-$Bi_2O_3/BiVO_4$ mixed-phase structure on a $BiVO_4$ electrocatalyst. The resulting photocurrent density of β-$Bi_2O_3/BiVO_4$ was approximately twice that of pristine $BiVO_4$ at 1.23 V_{RHE} for photoelectrochemical water splitting.[7]

Reconstructed structures of catalysts reportedly hamper their thermal catalytic performances.[8−10] For example, in high-temperature propane dehydrogenation reaction, Pt single atoms[11] and alloy nanoparticles[12] aggregate into larger nanoparticles, losing catalytic activity. Similarly, Pd nanoparticles rapidly lose catalytic activity by decomposing into inactive single atoms in high-temperature methane oxidation.[13] Notably, high-temperature and high-pressure can lead to changes in the catalyst composition,[14] crystal phase,[15] morphology,[16] and crystal size,[17] potentially exposing more abundant active sites or generating new ones during reactions. However, unlike electrocatalytic reactions, dynamic reconstruction of catalysts under high-temperature and high-pressure conditions is difficult to analyze *in situ* in thermal catalytic reactions, resulting in catalyst changes being compared only before and after the reaction.[18] So far, studies on the reconstruction processes of catalysts in thermal catalytic reactions are scarce, and notably, catalyst reconstruction that benefits thermal catalysis has not yet been reported.

This study presents a favorable reconstruction of $BiVO_4$ in the thermal catalytic selective oxidation of benzylic C−H of toluene. *In situ* characterization shows that the catalyst undergoes two reconstruction processes, sequentially forming $Bi/BiVO_4$ and $Bi_2O_3/BiVO_4$. Fabrication of an active $Bi_2O_3/$

Received: May 29, 2025
Revised: July 29, 2025
Accepted: August 13, 2025
Published: August 20, 2025

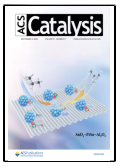

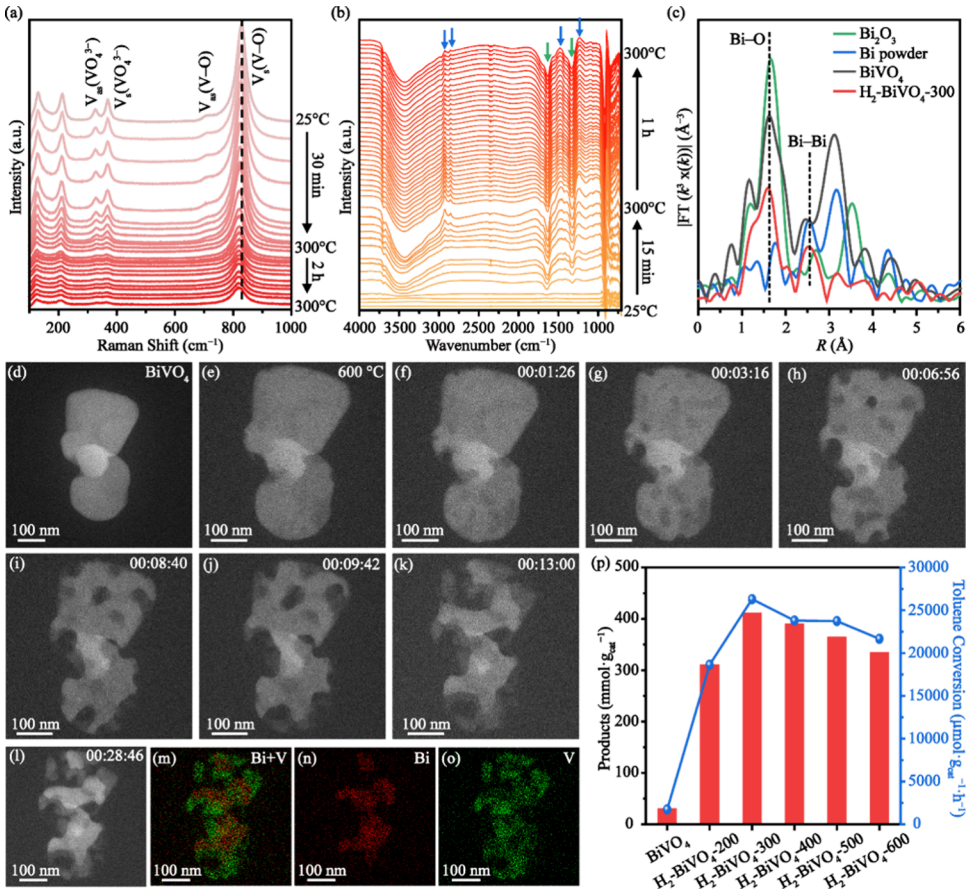

Figure 1. *In situ* (a) Raman and (b) FTIR spectra of the $BiVO_4$ species subjected to high-temperature treatment under a H_2 atmosphere. (c) Bi L_3-edge FT-EXAFS spectra. *In situ* STEM images of $BiVO_4$ at (d) 25 and (e) 600 °C under the H_2 atmosphere. (f–l) Time-dependent *in situ* STEM images of $BiVO_4$ at 600 °C under the H_2 atmosphere. (m–o) STEM/EDS mapping of $BiVO_4$ after H_2 reduction at 600 °C for 28 min and 46 s (as per panel (l)). (p) Product yield and toluene conversion obtained for thermal catalytic selective oxidation of benzylic C–H of toluene over the $BiVO_4$ and H_2–$BiVO_4$ species.

$BiVO_4$ interface results in a high toluene conversion of 26,300.00 μmol·g_{cat}^{-1}·h^{-1} and an unprecedented product yield of 410.00 mmol·g_{cat}^{-1}.

2. RESULTS AND DISCUSSION

A pristine $BiVO_4$ sheet, featuring distinct perovskite characteristic X-ray diffraction (XRD) peaks (JCPDS No. 83–1700; Figure S1), was synthesized by using the hydrothermal method. To improve its catalytic performance,[19] the $BiVO_4$ sheet was further treated by H_2 reduction at 200–600 °C. The XRD profile of H_2–$BiVO_4$ showed coexisting characteristic peaks of metallic Bi (JCPDS No. 85–1329) and $BiVO_4$ at a temperature of 300 °C (Figure S1). *In situ* Raman spectroscopy showed that the characteristic peaks at 321, 364, and 711 cm^{-1} gradually disappeared and a peak redshift occurred at 826 cm^{-1} in $BiVO_4$ under high-temperature H_2 reduction (Figure 1a). These peaks were assigned to the asymmetric and symmetric bending of VO_4^{3-} and to the asymmetric and symmetric stretching of V–O (Figure S2), which arise due to the dissolution and migration of Bi within the structure.[20] Fourier transform infrared (FTIR) spectroscopy showed that the typical $BiVO_4$ peak at 747 cm^{-1} gradually disappeared as the reduction temperature was increased (Figure S3), whereas a new peak appeared at 959 cm^{-1}, which was attributed to the terminal O stretching vibration of the V═O.[21] These observations implied the destruction of the Bi–O–V structure and the dissolution of Bi. Following high-temperature reduction with H_2, *in situ* FTIR spectroscopy showed the appearance of new peaks at 2927, 2857, 1486, and 1265 cm^{-1}, in addition to an inverted peak at 1323 cm^{-1} (Figure 1b), potentially due to destruction of the Bi–O and emergence of the strong affinity between H_2 and the generated metallic Bi particles. The normalized Bi L_3-edge X-ray absorption near-edge structure (XANES) profile of H_2–$BiVO_4$-300 was located between those of $BiVO_4$ and the Bi powder, indicating that some Bi^{3+} was reduced to Bi^0 (Figure S4).[22] The Fourier transforms of the extended X-ray absorption fine structure (FT-EXAFS) $k^3\chi$ data at the Bi L_3-edge directly confirmed the existence of metallic Bi particles in H_2–$BiVO_4$-300, wherein the peak at 2.53 Å was attributed to the Bi–Bi (Figure 1c).[23] The presence of metallic Bi particles in H_2–$BiVO_4$-300 was further confirmed by the wavelet transform contour plots, which indicated the dominance of the Bi–Bi structure at 12.8 $Å^{-1}$ (Figure S5).[23]

Scanning electron microscopy (SEM) images confirmed the formation of metallic Bi particles in H_2–$BiVO_4$ during high-temperature H_2 reduction (Figure S6). The dynamic evolution of the Bi dissolution process and subsequent aggregation into metallic Bi particles was monitored using *in situ* scanning transmission electron microscopy (STEM). However, no significant changes were observed on the surface of the $BiVO_4$ sheet at a reduction temperature below 550 °C (Figure

https://doi.org/10.1021/acscatal.5c03644
ACS Catal. 2025, 15, 15387–15394

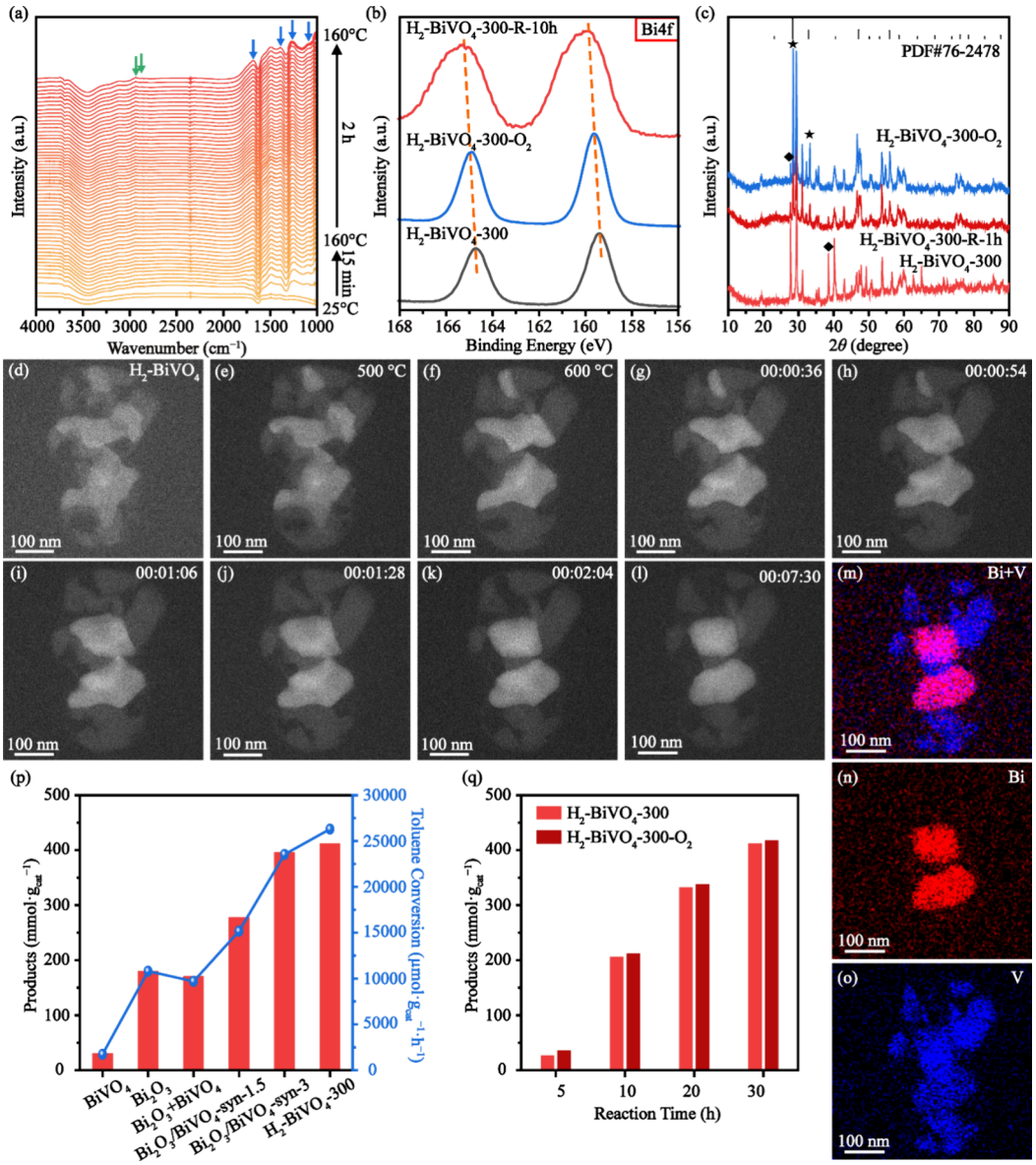

Figure 2. (a) *In situ* FTIR spectra of the H_2−$BiVO_4$-300 specimen subjected to high-temperature treatment under an O_2 atmosphere. (b) XPS Bi 4f results were obtained for H_2−$BiVO_4$-300, H_2−$BiVO_4$-300-O_2, and H_2−$BiVO_4$-300-R-10h. (c) XRD characterization of H_2−$BiVO_4$-300, H_2−$BiVO_4$-300-R-1h, and H_2−$BiVO_4$-300-O_2. Star indicates the characteristic peaks belonging to Bi_2O_3. Diamond indicates the characteristic peaks belonging to metallic Bi particles. *In situ* STEM images of the reduced $BiVO_4$ undergoing high-temperature reoxidation under an O_2 atmosphere at (d) 25 °C, (e) 500 °C, and (f) 600 °C. (g−l) Time-dependent *in situ* STEM images of the reduced $BiVO_4$ undergoing O_2 reoxidation at 600 °C. (m−o) STEM/EDS mapping images of the reduced $BiVO_4$ after O_2 reoxidation at 600 °C for 7 min and 30 s (as per panel (l)). (p) Product yield and toluene conversion obtained over the $BiVO_4$, Bi_2O_3, Bi_2O_3 + $BiVO_4$, Bi_2O_3/$BiVO_4$-syn-1.5, Bi_2O_3/$BiVO_4$-syn-3, and H_2−$BiVO_4$-300 species. (q) Time-dependent product yield obtained for H_2−$BiVO_4$-300 and H_2−$BiVO_4$-300-O_2.

S7). By contrast, Bi dissolution occurred at 300 °C in a tube furnace, as the *in situ* STEM system remained under a low partial pressure of H_2. Additionally, when the reduction temperature reached 600 °C, obvious defects caused by the dissolution of Bi appeared on the surface of the $BiVO_4$ sheet (Figure 1d,e). The density of defects increased with reduction time, and the significant aggregation of Bi particles was observed up to 13 min (Figure 1f−l). In STEM/energy-dispersive X-ray spectroscopy (EDS) mapping images, large amounts of Bi were concentrated at the positions corresponding to the Bi particles, while V showed an average distribution over $BiVO_4$ (Figure 1m−o). These results indicate that $BiVO_4$ underwent reconstruction to form Bi/$BiVO_4$ (H_2−$BiVO_4$) after high-temperature H_2 reduction.

Subsequently, the catalytic performance of each catalyst was compared using the model reaction of thermal catalytic selective oxidation of benzylic C−H of toluene to yield benzyl alcohol, benzaldehyde, benzoic acid, and benzyl benzoate. All the catalysts showed similar product selectivity (approximately 55%; Figure S8 and Table S1). However, H_2−$BiVO_4$ showed an ultrahigh toluene conversion (over 18,000.00 μmol·g_{cat}^{-1}·h^{-1}), compared to that of the pristine $BiVO_4$ (1733.33 μmol·g_{cat}^{-1}·h^{-1}). As a result, all of the H_2−$BiVO_4$ provided a product yield exceeding 300.00 mmol·g_{cat}^{-1}, while the pristine $BiVO_4$ gave a poor product yield of only 29.00 mmol·g_{cat}^{-1} (Figure 1p). Notably, H_2−$BiVO_4$-300 exhibited the best product yield (410.00 mmol·g_{cat}^{-1}) and toluene conversion (26,300.00 μmol·g_{cat}^{-1}·h^{-1}), which are 14.14- and 15.17-fold greater

https://doi.org/10.1021/acscatal.5c03644
ACS Catal. 2025, 15, 15387−15394

than those of the pristine $BiVO_4$, respectively. To the best of our knowledge, this is the highest product yield reported for the thermal catalytic selective oxidation of benzylic C−H of toluene, even higher than those obtained using solvents (Table S2). In addition, H_2−$BiVO_4$-300 retained over 85% of its performance after five cycles (Figure S9), indicating excellent stability. The slight decrease in activity may be ascribed to carbon deposition on the H_2−$BiVO_4$-300 surface (Figure S10).

Notably, metallic Bi particles can be easily oxidized to Bi_2O_3 under high-temperature oxidation conditions.[24] *In situ* FTIR spectra of H_2−$BiVO_4$-300, recorded under an O_2 atmosphere, showed some new peaks at 1686, 1389, 1273, and 1015 cm^{-1} (Figure 2a). The intensity of the peak at 2927 cm^{-1} decreased, while the shape of the peak at 2857 cm^{-1} was inverted (Figure 2a). These indicate that the affinity between metallic Bi particles and H_2 was disrupted due to the oxidation of metallic Bi. Interestingly, *in situ* FTIR spectra obtained under an O_2/toluene mixed atmosphere showed the same results as those under an O_2 atmosphere, with the exception of an additional characteristic peak at 2531 cm^{-1} attributed to toluene (Figure S11).[25] This indicates that the reconstruction of H_2−$BiVO_4$-300 in the reaction was mainly due to the action of O_2. X-ray photoelectron spectroscopy (XPS) showed that both Bi 4f peaks of O_2/toluene-treated H_2−$BiVO_4$-300 (H_2−$BiVO_4$-300-R) and O_2-treated H_2−$BiVO_4$-300 (H_2−$BiVO_4$-300-O_2) exhibited a positive shift compared to that of fresh H_2−$BiVO_4$-300 (Figure 2b), indicating that metallic Bi was oxidized.[26] The observation of a characteristic XRD peak (JCPDS No. 76−2478) corresponding to Bi_2O_3 further confirmed such oxidation of metallic Bi (Figure 2c and Figure S12). Both H_2−$BiVO_4$-300-R and H_2−$BiVO_4$-300-O_2 exhibited a mixed crystal phase of Bi_2O_3 and $BiVO_4$, whereas the O_2/toluene-treated $BiVO_4$ ($BiVO_4$-R) did not, confirming the formation of an interface in the secondary reconstruction (Figure 2c and Figure S13).

The SEM and TEM/EDS images recorded for H_2−$BiVO_4$-300-R and H_2−$BiVO_4$-300-O_2 showed that H_2−$BiVO_4$ underwent the same secondary reconstruction process while $BiVO_4$-R did not (Figures S14−S16). The dynamic evolution of H_2−$BiVO_4$ under high-temperature O_2 oxidation was monitored using *in situ* STEM. The morphology of H_2−$BiVO_4$ changed significantly at treatment temperature above 600 °C (Figure 2d−f and Figure S17), consistent with the trend observed during H_2 reduction. Upon increasing the oxidation time, the Bi particles continuously shrank and aggregated, attaining relative stability at 4 min 6 s (Figure 2g−l and Figure S18). STEM/EDS mapping showed that Bi was highly concentrated at the Bi particle positions after oxidation, whereas V remained evenly distributed over $BiVO_4$ (Figure 2m−o). These results indicated that H_2−$BiVO_4$ underwent a new reconstruction to Bi_2O_3/$BiVO_4$ after high-temperature oxidation. STEM/EDS linear scanning demonstrated a distinct interface between the Bi region and $BiVO_4$ components (Figure S19). Compared with the Bi/V signal intensity ratio obtained from Line 1 in H_2−$BiVO_4$, the relative intensity of the Bi signal from Line 2 in H_2−$BiVO_4$−O_2 was strengthened after high-temperature oxidation. The O/V intensity ratio at the interface in Line 2 was higher than that in Line 1, which was attributed to the formation of Bi_2O_3 under high-temperature oxidation conditions.

To reveal the role of Bi_2O_3 in the thermal reaction, Bi_2O_3 and Bi_2O_3/$BiVO_4$-syn were synthesized using the hydrothermal method (Figure S20). Bi_2O_3 provided a product yield of 178.00 mmol·g_{cat}^{-1} and toluene conversion of 10,800.00 μmol·g_{cat}^{-1}·h^{-1}, which are 6.14- and 6.23-fold higher than those of the pristine $BiVO_4$, respectively (Figure 2p and Table S1). Bi_2O_3/$BiVO_4$-syn exhibited a superior catalytic performance to both Bi_2O_3 and $BiVO_4$ (Figure 2p, Figure S21, and Table S1), indicating the existence of synergy between Bi_2O_3 and $BiVO_4$. Particularly, the product yield of Bi_2O_3/$BiVO_4$-syn-3 (394.00 mmol·g_{cat}^{-1}) was approximately equal to that of H_2−$BiVO_4$-300 (Figure 2p). Furthermore, when the fresh H_2−$BiVO_4$-300 was preoxidized at 160 °C for 5 h to obtain H_2−$BiVO_4$-300-O_2, a superior catalytic performance was achieved, with a product yield of 416.00 mmol·g_{cat}^{-1} and toluene conversion of 26466.67 μmol·g_{cat}^{-1}·h^{-1} (Figure 2q). This was attributed to the fact that Bi_2O_3 was preformed in H_2−$BiVO_4$-300-O_2, rather than being generated during the reaction. Notably, the physically mixed Bi_2O_3+$BiVO_4$ exhibited a poorer catalytic performance (169.00 mmol·g_{cat}^{-1}; 9700.00 μmol·g_{cat}^{-1}·h^{-1}) than that of Bi_2O_3 (Figure 2p and Table S1). Moreover, the activity of H_2−$BiVO_4$-300 decreased after dilute nitric acid etching (326.00 mmol·g_{cat}^{-1}; 20,166.67 μmol·g_{cat}^{-1}·h^{-1}; Table S1), indicating that Bi vacancies were not the active sites for this reaction.[27,28] Therefore, the enhanced catalytic performance is expected to be relevant to the generated interface between Bi_2O_3 and $BiVO_4$.

Electron transport during the reaction was subsequently explored to reveal the role of the Bi_2O_3/$BiVO_4$ interface in the thermal reaction.[29] Initially, a quenching experiment was conducted to identify the active species. As shown in Figure 3a, the catalytic activity of H_2−$BiVO_4$-300 decreased significantly upon the addition of potassium persulfate, ammonium oxalate, and *p*-benzoquinone as electron, hole, and superoxide radical quenchers, respectively, confirming the key roles of these active

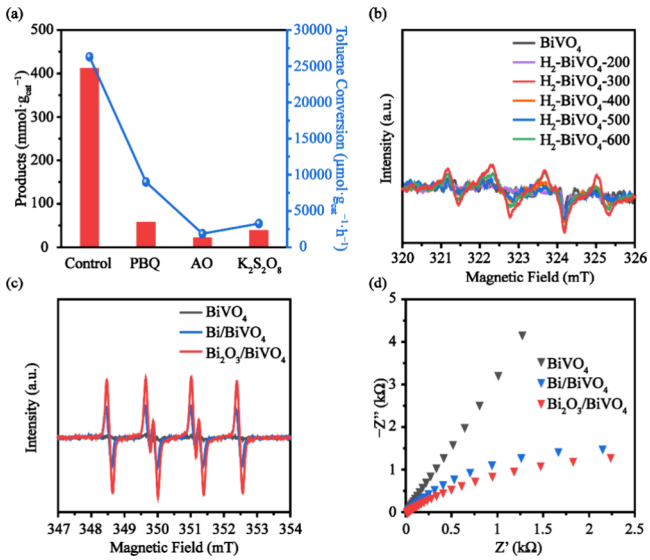

Figure 3. (a) Product yield and toluene conversion over H_2−$BiVO_4$-300 upon the addition of a quencher. *p*-Benzoquinone (PBQ) was added as a superoxide radical quencher, ammonium oxalate (AO) was added as a hole quencher, and potassium persulfate ($K_2S_2O_8$) was added as an electron quencher. (b) EPR spectra of the superoxide radicals generated in $BiVO_4$ and H_2−$BiVO_4$. (c) EPR spectra of the superoxide radical generated in $BiVO_4$, Bi/$BiVO_4$, and Bi_2O_3/$BiVO_4$, where H_2−$BiVO_4$-300 is denoted as Bi/$BiVO_4$ and H_2−$BiVO_4$-300-O_2 is denoted as Bi_2O_3/$BiVO_4$. (d) EIS spectra of $BiVO_4$, Bi/$BiVO_4$, and Bi_2O_3/$BiVO_4$.

https://doi.org/10.1021/acscatal.5c03644
ACS Catal. 2025, 15, 15387−15394

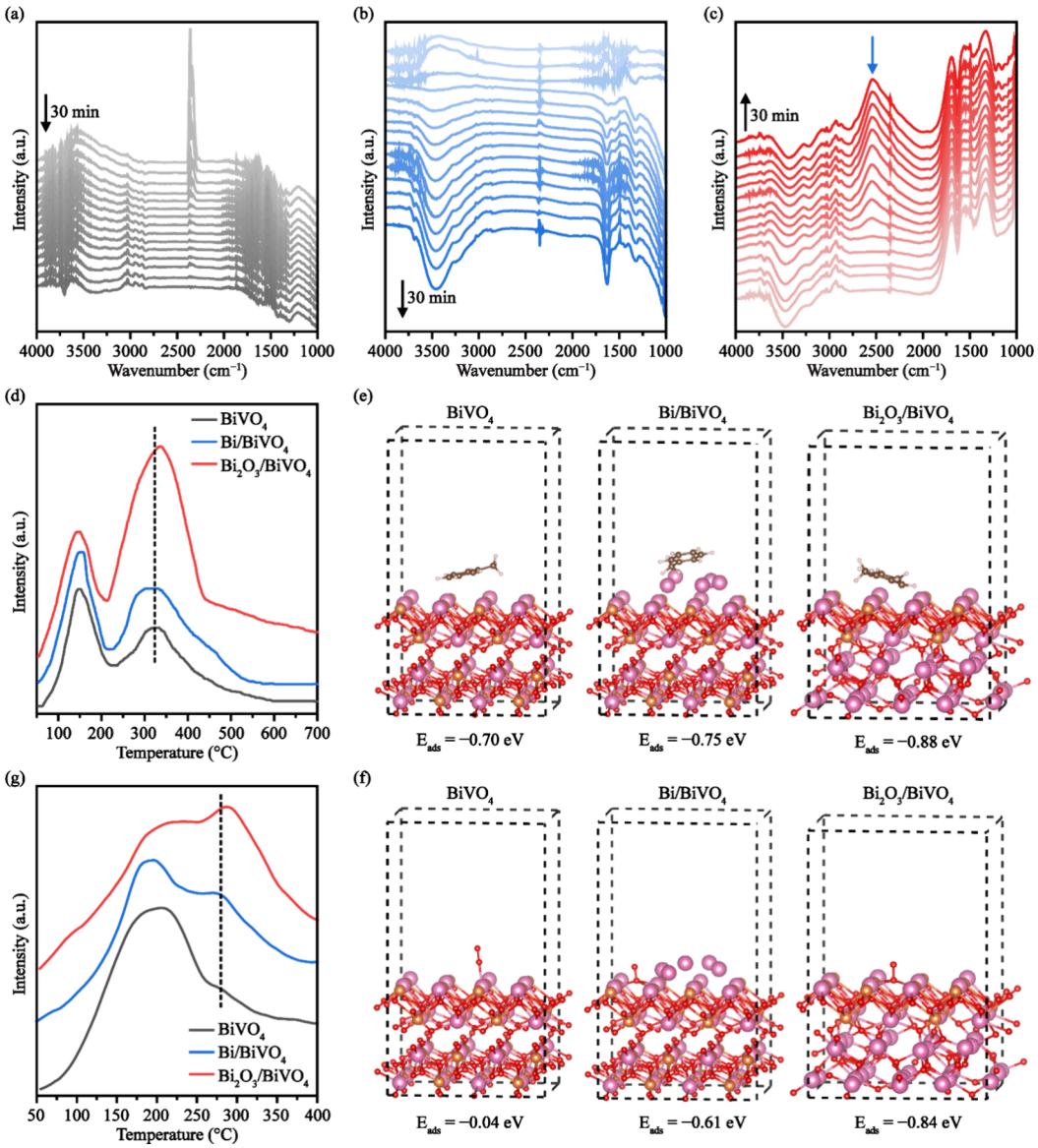

Figure 4. *In situ* FTIR spectra of toluene adsorption on (a) $BiVO_4$, (b) $Bi/BiVO_4$, and (c) $Bi_2O_3/BiVO_4$. H_2−$BiVO_4$-300 is denoted as $Bi/BiVO_4$ and H_2−$BiVO_4$-300-O_2 is denoted as $Bi_2O_3/BiVO_4$. (d) Toluene-TPD results for $BiVO_4$, $Bi/BiVO_4$, and $Bi_2O_3/BiVO_4$. (e) Optimized geometric structures and corresponding toluene adsorption energies on $BiVO_4$, $Bi/BiVO_4$, and $Bi_2O_3/BiVO_4$. (f) Optimized geometric structures and corresponding O_2 adsorption energies on the $BiVO_4$, $Bi/BiVO_4$, and $Bi_2O_3/BiVO_4$. (g) O_2-TPD results for $BiVO_4$, $Bi/BiVO_4$, and $Bi_2O_3/BiVO_4$.

species in thermal catalytic selective oxidation of benzylic C−H.[30,31] Electron paramagnetic resonance (EPR) spectra of H_2−$BiVO_4$-300 exhibited the strongest superoxide radical ($\bullet O_2^-$) signal, corroborating its highest catalytic performance (Figure 3b). Compared with $BiVO_4$ and $Bi/BiVO_4$, $Bi_2O_3/BiVO_4$ exhibited the strongest $\bullet O_2^-$ signal, implying the best charge transport properties (Figure 3c). Furthermore, electrochemical impedance spectroscopy (EIS) demonstrated that $Bi_2O_3/BiVO_4$ gave the smallest high-frequency semicircle in the Nyquist plot than both $BiVO_4$ and $Bi/BiVO_4$ (Figure 3d), indicating that $Bi_2O_3/BiVO_4$ exhibited the lowest degree of resistance during charge transport.[32] Therefore, the increase in the activity was attributed to excellent charge transport at the $Bi_2O_3/BiVO_4$ interface, which generated a greater number of active species. Based on this result, along with the product generation order of benzaldehyde, benzyl alcohol, benzoic acid, and benzyl benzoate, a product generation pathway was proposed (Figures S22 and S23),[33,34] and density functional theory (DFT) calculations confirmed such a free radical process (Figures S23 and S24).[35]

Toluene adsorption over the catalysts was investigated by using *in situ* FTIR spectroscopy. Compared to $BiVO_4$ and $Bi/BiVO_4$, a distinct characteristic peak corresponding to toluene was observed at 2531 cm^{-1} for $Bi_2O_3/BiVO_4$ (Figure 4a−c), indicting its strongest adsorption capacity for toluene. In agreement with the adsorption capacity, $Bi_2O_3/BiVO_4$ also exhibited a higher toluene desorption temperature than $BiVO_4$ and $Bi/BiVO_4$ in the toluene temperature-programmed desorption experiments (Toluene-TPD) (Figure 4d). This was further confirmed by using DFT calculations (Figure 4e and Figure S24). The toluene adsorption energy was found to increase in the following order: $Bi_2O_3/BiVO_4$ (E_{ads} = −0.88 eV) < $Bi/BiVO_4$ (E_{ads} = −0.75 eV) < $BiVO_4$ (E_{ads} = −0.70 eV). Interestingly, DFT calculations also suggested the excellent adsorption of O_2 on the $Bi_2O_3/BiVO_4$. The O_2 adsorption energy increased in the following order: $Bi_2O_3/$

https://doi.org/10.1021/acscatal.5c03644
ACS Catal. 2025, 15, 15387−15394

$BiVO_4$ (E_{ads} = −0.84 eV) < Bi/$BiVO_4$ (E_{ads} = −0.61 eV) < $BiVO_4$ (E_{ads} = −0.04 eV) (Figure 4f). In the O_2 temperature-programmed desorption experiments (O_2-TPD), Bi_2O_3/$BiVO_4$ demonstrated the highest desorption temperature in the high-temperature zone, corresponding to the superior chemical adsorption of O_2 on Bi_2O_3/$BiVO_4$ compared on the $BiVO_4$ and Bi/$BiVO_4$ (Figure 4g). Obviously, the enhanced adsorption capacities of Bi_2O_3/$BiVO_4$ toward toluene and O_2 also played crucial roles in enhancing its catalytic performance of selective oxidation of benzylic C−H.

3. CONCLUSIONS

In summary, this study demonstrated the occurrence of a favorable reconstruction process during a thermal catalytic reaction. $BiVO_4$ undergoes its first reconstruction to form Bi/$BiVO_4$, which subsequently undergoes a secondary reconstruction during thermal selective oxidation of benzylic C−H of toluene to generate Bi_2O_3/$BiVO_4$. The Bi_2O_3/$BiVO_4$ interface exhibits excellent adsorption properties for toluene and O_2, in addition to promoting charge transport to generate more abundant active species, thereby significantly enhancing the catalytic activity. Such favorable reconstruction can be a promising application for unstable catalysts, particularly with respect to achieving superior thermal catalytic activities.

4. METHODS

4.1. Catalyst Preparation. *Preparation of the $BiVO_4$ Sheet.* The $BiVO_4$ sheet catalyst was synthesized by using a hydrothermal method. More specifically, $Bi(NO_3)_3{\cdot}5H_2O$ (5 mmol) and sodium dodecylbenzenesulfonate (0.72 mmol) were sequentially dissolved in dilute nitric acid (4 M, 10 mL) and stirred for 30 min to form solution A. In addition, NH_4VO_3 (5 mmol) was dissolved in an aqueous NaOH solution (2 M, 10 mL) and stirred for 10 min to form solution B. Solution A was then added dropwise to solution B, and the pH of the mixture was adjusted to 7 using an aqueous NaOH solution (2 M). After it was stirred continuously for 30 min to form a suspension, the suspension was transferred to a hydrothermal reactor (HTG-100-SS1, Anhui Kemi Machinery Technology Co., Ltd.) and heated at 200 °C for 1.5 h. After this time, the reaction mixture was cooled naturally to room temperature and centrifuged to obtain a solid precipitate, which was washed with anhydrous ethanol and deionized water prior to drying at 100 °C.

Preparation of the H_2−$BiVO_4$ Catalyst. The obtained $BiVO_4$ sheet was reduced at different temperatures (200, 300, 400, 500, and 600 °C) for 2 h in a H_2 atmosphere to obtain H_2−$BiVO_4$-X (X corresponds to the reduction temperature, X = 200, 300, 400, 500, and 600).

Preparation of the Bi_2O_3 Catalyst. The preparation method of Bi_2O_3 was the same as that of the $BiVO_4$ sheet, except that no NH_4VO_3 was added.

Preparation of the Bi_2O_3/$BiVO_4$-syn Catalyst. The preparation method of Bi_2O_3/$BiVO_4$-syn-X (X represents the molar ratio of Bi to V, with corresponding values of 1.5, 2, 2.4, 3, 3.2, and 4) was the same as that of the $BiVO_4$ sheet, except that the amount of $Bi(NO_3)_3{\cdot}5H_2O$ added was adjusted to 7.5, 10.0, 12.0, 15.0, 16.0, and 20.0 mmol.

Preparation of the H_2−$BiVO_4$-300-O_2 Catalyst. The obtained H_2−$BiVO_4$-300 was oxidized at 160 °C for 5 h in an O_2 atmosphere to obtain H_2−$BiVO_4$-300-O_2.

4.2. Characterization. XRD spectra were measured and collected using an X'Pert PRO (PANalytical) powder diffractometer using a Cu Kα radiation source with a wavelength λ of 0.15418 nm, test voltage of 40 kV, and current of 40 mA. The Raman spectrum was measured by a LabRAM HR EVOLUTION spectrometer. The excitation wavelength was 532 nm, and the scanning range was 100−1000 cm^{-1}. In the *in situ* Raman experiment, the pristine $BiVO_4$ was first pretreated with N_2 at 100 °C for 30 min to remove adsorbed impurities, then cooled to 25 °C. After that, it was heated to 300 °C within 30 min and maintained for 2 h in a H_2 atmosphere. Raman spectra were collected intermittently in a H_2 atmosphere. FTIR spectroscopy was conducted on an INVENIO-R spectrometer (Bruker, Germany) in the range of 400−4000 cm^{-1}. *In situ* FTIR spectroscopy was conducted with an MCT (mercury cadmium telluride) detector. In the *in situ* reconstruction experiment, the catalyst was initially pretreated with N_2 at 100 °C for 30 min to remove any adsorbed impurities and then cooled to 25 °C. Subsequently, it was heated to 300 °C over 15 min and maintained at 300 °C for 1 h under an H_2 atmosphere. The *in situ* FTIR spectra were collected intermittently in a H_2 atmosphere. Subsequently, the catalyst was treated with N_2 at 100 °C for 30 min and cooled to 25 °C. It was then heated to 160 °C over 15 min and maintained at 160 °C for 2 h under an O_2 (or an O_2/Toluene) atmosphere. The *in situ* FTIR spectra were collected intermittently in the O_2 (or O_2/Toluene) atmosphere. In the toluene adsorption experiment, the catalyst was initially pretreated with N_2 at 100 °C for 30 min to remove any adsorbed impurities and then cooled to 25 °C. Subsequently, toluene gas was continuously introduced for 30 min, and the *in situ* FTIR spectra were collected intermittently. The EXAFS and XANES data at the Bi L-edge was collected at the 1W1B beamline at the BSRF (Beijing Synchrotron Radiation Facility, China). The SEM and SEM/EDS measurements were conducted using an SU-8020 electron microscope (Hitachi, Japan). The TEM/EDS measurements were carried out using field emission transmission electron microscope combined with energy dispersive X-ray spectrometry (JEM-2100 F, JEOL, Japan). The *in situ* STEM experiment was carried out in a JEOL JEM F200 microscope at 200 kV with a DENS heating holder. STEM images and STEM/EDS were acquired after the sample was heated to the target temperature in a H_2 or O_2 atmosphere. The XPS was carried out using an AXIS Supra photoelectron spectrometer (Kratos analytical company) equipped with an Al Kα excitation source. The peak positions were corrected according to the position of C 1s at 284.8 eV. The toluene-TPD experiments were performed using an Autochem 2720 chemical adsorption instrument at a catalyst dosage of 100 mg. Prior to testing, the catalyst was pretreated with He at 250 °C for 1 h with a flow rate of 30 mL·min^{-1} to remove any adsorbed impurities and then cooled to 50 °C. Subsequently, the He flow was switched to toluene at a flow rate of 30 mL·min^{-1} and maintained for 1 h. After this adsorption period, the toluene flow was switched back to He at a flow rate of 30 mL·min^{-1} and maintained for 30 min. Finally, the temperature was increased from 50 to 800 °C at a heating rate of 10 °C·min^{-1}, and the signal was collected by using a thermal conductivity (TCD) detector. The O_2-TPD was performed on an Autochem 2720 chemical adsorption instrument with a catalyst dosage of 100 mg. The detailed operation was the same as that of Toluene-TPD, except that 5% O_2/He was used to replace

https://doi.org/10.1021/acscatal.5c03644
ACS Catal. 2025, 15, 15387−15394

toluene gas. The $\bullet O_2^-$ tests were measured using an EPR spectrometer (E500, Bruker, Germany) at room temperature. The catalyst was dispersed in dimethyl sulfoxide (DMSO), added with 5, 5-dimethyl-1-pyrroline N-oxide (DMPO) capture agent, and then put into a paramagnetic tube for testing by capillary encapsulation. The EIS measurements were performed in the frequency range of 100 mHz to 100 kHz.

4.3. Evaluation of the Catalytic Performance. *Thermal Catalytic Selective Oxidation of Benzylic C−H of Toluene.* The thermal catalytic selective oxidation of benzylic C−H of toluene was performed in an autoclave (NSVP25-P3-T2-SS1-SV, Anhui Kemi Machinery Technology Co., Ltd.). Specifically, toluene (15 mL) and the catalyst (30 mg) were added to the autoclave, and the autoclave was repeatedly purged 5 times with high-purity O_2 (0.5 MPa) to ensure a pure O_2 atmosphere. Subsequently, the autoclave was filled with 0.5 MPa O_2 and heated to 160 °C, at which point the O_2 in the autoclave was replenished to 1 MPa and maintained constant throughout the experiment. Finally, the magnetic stirrer was turned on, and the rotational speed was set to 1000 rpm. Samples were taken before the start of heating and after the end of the 30 h reaction for analysis by gas chromatography (GC; 2010Plus, Shimadzu, Japan) with a flame ionization (FID) detector.

For the quenching experiment, each quencher (*p*-benzoquinone, ammonium oxalate, and potassium persulfate) and catalyst were added simultaneously, and the subsequent steps were completely consistent with the activity test.

4.4. DFT Calculations. All of the calculations are performed in the framework of density functional theory with the projector augmented plane-wave method, as implemented in the Vienna ab initio simulation package. The generalized gradient approximation proposed by Perdew, Burke, and Ernzerhof is selected for the exchange-correlation potential. The long-range van der Waals interaction is described by the DFT-D3 approach. The cutoff energy for plane wave is set to 400 eV. The energy criterion is set to 10^{-5} eV in iterative solution of the Kohn−Sham equation. A vacuum layer of 15 Å is added perpendicular to the sheet to avoid artificial interaction between periodic images. The Brillouin-zone integrations were performed using a Gamma-point-only grid. All of the structures are relaxed until the residual forces on the atoms have declined to less than 0.05 eV/Å.

■ ASSOCIATED CONTENT

Supporting Information

The Supporting Information is available free of charge at https://pubs.acs.org/doi/10.1021/acscatal.5c03644.

Experimental section, details of the characterization, and DFT calculations (PDF)

■ AUTHOR INFORMATION

Corresponding Authors

Xiaozhi Liu − *Beijing National Laboratory for Condensed Matter Physics, Institute of Physics, Chinese Academy of Sciences, Beijing 100190, China;* orcid.org/0000-0001-8647-8694; Email: liuxz@iphy.ac.cn

Maoyong Song − *Key Laboratory of Environmental Nanotechnology and Health Effects, Research Center for Eco-Environmental Sciences, Chinese Academy of Sciences, Beijing 100085, China; State Key Laboratory of Environmental Chemistry and Ecotoxicology, Research Center for Eco-Environmental Sciences, Chinese Academy of Sciences, Beijing 100085, China;* orcid.org/0000-0002-6776-4705; Email: smsong@rcees.ac.cn

Authors

Cheng Chen − *Key Laboratory of Environmental Nanotechnology and Health Effects, Research Center for Eco-Environmental Sciences, Chinese Academy of Sciences, Beijing 100085, China; State Key Laboratory of Environmental Chemistry and Ecotoxicology, Research Center for Eco-Environmental Sciences, Chinese Academy of Sciences, Beijing 100085, China;* orcid.org/0000-0002-9439-0227

Yifan Xu − *Nanjing Institute of Environmental Sciences, Ministry of Ecology and Environment of China, Nanjing 210042, China*

Chunyan Ma − *Key Laboratory of Environmental Nanotechnology and Health Effects, Research Center for Eco-Environmental Sciences, Chinese Academy of Sciences, Beijing 100085, China; State Key Laboratory of Environmental Chemistry and Ecotoxicology, Research Center for Eco-Environmental Sciences, Chinese Academy of Sciences, Beijing 100085, China*

Bolei Chen − *Key Laboratory of Environmental Nanotechnology and Health Effects, Research Center for Eco-Environmental Sciences, Chinese Academy of Sciences, Beijing 100085, China; State Key Laboratory of Environmental Chemistry and Ecotoxicology, Research Center for Eco-Environmental Sciences, Chinese Academy of Sciences, Beijing 100085, China;* orcid.org/0000-0001-8552-3334

Fanglan Geng − *State Key Laboratory of Environmental Chemistry and Ecotoxicology, Research Center for Eco-Environmental Sciences, Chinese Academy of Sciences, Beijing 100085, China*

Guibin Jiang − *State Key Laboratory of Environmental Chemistry and Ecotoxicology, Research Center for Eco-Environmental Sciences, Chinese Academy of Sciences, Beijing 100085, China;* orcid.org/0000-0002-6335-3917

Complete contact information is available at: https://pubs.acs.org/10.1021/acscatal.5c03644

Author Contributions

#C.C., Y.X., and C.M. contributed equally to this work.

Notes

The authors declare no competing financial interest.

■ ACKNOWLEDGMENTS

This work was supported by the National Natural Science Foundation of China (Grant Nos. 22125606 and 22241604), the Stretegic Priority Research Program of the Chinese Academy of Sciences (XDB0750300), and the Chinese Academy of Sciences Project for Young Scientists in Basic Research (YSBR-086).

■ REFERENCES

(1) Lin, C.; Li, J. L.; Li, X.; Yang, S.; Luo, W.; Zhang, Y.; Kim, S. H.; Kim, D. H.; Shinde, S. S.; Li, Y. F.; Liu, Z. P.; Jiang, Z.; Lee, J. H. In-situ reconstructed Ru atom array on α-MnO_2 with enhanced performance for acidic water oxidation. *Nat. Catal.* **2021**, *4*, 1012−1023.

(2) Fabbri, E.; Nachtegaal, M.; Binninger, T.; Cheng, X.; Kim, B. J.; Durst, J.; Bozza, F.; Graule, T.; Schaublin, R.; Wiles, L.; Pertoso, M.; Danilovic, N.; Ayers, K. E.; Schmidt, T. J. Dynamic surface self-

reconstruction is the key of highly active perovskite nano-electrocatalysts for water splitting. *Nat. Mater.* **2017**, *16*, 925−931.
(3) Lv, H.; Lin, L.; Zhang, X.; Li, R.; Song, Y.; Matsumoto, H.; Ta, N.; Zeng, C.; Fu, Q.; Wang, G.; Bao, X. Promoting exsolution of RuFe alloy nanoparticles on $Sr_2Fe_{1.4}Ru_{0.1}Mo_{0.5}O_{6-\delta}$ via repeated redox manipulations for CO_2 electrolysis. *Nat. Commun.* **2021**, *12*, 5665.
(4) Okatenko, V.; Loiudice, A.; Newton, M. A.; Stoian, D. C.; Blokhina, A.; Chen, A. N.; Rossi, K.; Buonsanti, R. Alloying as a strategy to boost the stability of copper nanocatalysts during the electrochemical CO_2 reduction reaction. *J. Am. Chem. Soc.* **2023**, *145*, 5370−5383.
(5) Jia, G.; Wang, Y.; Sun, M.; Zhang, H.; Li, L.; Shi, Y.; Zhang, L.; Cui, X.; Lo, B. T. W.; Huang, B.; Yu, J. C. Size effects of highly dispersed bismuth nanoparticles on electrocatalytic reduction of carbon dioxide to formic acid. *J. Am. Chem. Soc.* **2023**, *145*, 14133−14142.
(6) Pi, Y.; Shao, Q.; Zhu, X.; Huang, X. Dynamic structure evolution of composition segregated iridium-nickel rhombic dodecahedra toward efficient oxygen evolution electrocatalysis. *ACS Nano* **2018**, *12*, 7371−7379.
(7) Lee, S.; Song, J.; Jo, Y. R.; Choi, K. S.; Lee, J.; Seo, S.; Kim, T. L.; Jang, H. W.; Jeon, C.; Kim, B. J.; Kim, B.; Lee, S. In situ growth of nanostructured $BiVO_4$−Bi_2O_3 mixed-phase via nonequilibrium deposition involving metal exsolution for enhanced photoelectrochemical water splitting. *ACS Appl. Mater. Interface* **2019**, *11*, 44069−44076.
(8) Nakaya, Y.; Hirayama, J.; Yamazoe, S.; Shimizu, K.; Furukawa. Single-atom Pt in intermetallics as an ultrastable and selective catalyst for propane dehydrogenation. *Nat. Commun.* **2020**, *11*, 2838.
(9) Zhang, Z.; Zhu, Y.; Asakura, H.; Zhang, B.; Zhang, J.; Zhou, M.; Han, Y.; Tanaka, T.; Wang, A.; Zhang, T.; Yan, N. Thermally stable single atom Pt/m-Al_2O_3 for selective hydrogenation and CO oxidation. *Nat. Commun.* **2017**, *8*, 16100.
(10) Yang, Y.; Wang, G.; Zheng, P.; Dang, F.; Han, J. Carbon deposits during catalytic combustion of toluene on Pd−Pt-based catalysts. *Catal. Sci. Technol.* **2020**, *10*, 2452−2461.
(11) Duan, S.; Wang, R.; Liu, J. Stability investigation of a high number density Pt_1/Fe_2O_3 single-atom catalyst under different gas environments by HAADF-STEM. *Nanotechnology* **2018**, *29*, No. 204002.
(12) Sun, G.; Zhao, Z. J.; Mu, R.; Zha, S.; Li, L.; Chen, S.; Zang, K.; Luo, J.; Li, Z.; Purdy, S. C.; Kropf, A. J.; Miller, J. T.; Zeng, L.; Gong, J. Breaking the scaling relationship via thermally stable Pt/Cu single atom alloys for catalytic dehydrogenation. *Nat. Commun.* **2018**, *9*, 4454.
(13) Goodman, E. D.; Johnston-peck, A. C.; Dietze, E. M.; Wrasman, C. J.; Hoffman, A. S.; Abild-Pedersen, F.; Bare, S. R.; Plessow, P. N.; Cargnello, M. Catalyst deactivation via decomposition into single atoms and the role of metal loading. *Nat. Catal.* **2019**, *2*, 748−755.
(14) Yin, H.; Dong, F.; Wang, D.; Li, J. Coupling Cu single atoms and phase junction for photocatalytic CO_2 reduction with 100% CO selectivity. *ACS Catal.* **2022**, *12*, 14096−14105.
(15) Bao, H.; Zhang, W.; Hua, Q.; Jiang, Z.; Yang, J. Crystal-plane-controlled surface restructuring and catalytic performance of oxide nanocrystals. *Angew. Chem., Int. Ed.* **2011**, *50*, 12294−12298.
(16) Hill, A. J.; Seo, C. Y.; Chen, X.; Bhat, A.; Fisher, G. B.; Lenert, A.; Schwank, J. W. Thermally induced restructuring of Pd@CeO_2 and Pd@SiO_2 nanoparticles as a strategy for enhancing low-temperature catalytic activity. *ACS Catal.* **2020**, *10*, 1731−1741.
(17) Qu, Y.; Li, Z.; Chen, W.; Lin, Y.; Yuan, T.; Yang, Z.; Zhao, C.; Wang, J.; Zhao, C.; Wang, X.; Zhou, F.; Zhuang, Z.; Wu, Y.; Li, Y. Direct transformation of bulk copper into copper single sites via emitting and trapping of atoms. *Nat. Catal.* **2018**, *1*, 781−786.
(18) Jones, J.; Xiong, H.; Delariva, A. T.; Peterson, E. J.; Pham, H.; Challa, S. R.; Qi, G.; OH, S.; Wiebenga, M. H.; Hernandez, X. I. P.; Wang, Y.; Datye, A. K. Thermally stable single-atom platinum-on-ceria catalysts via atom trapping. *Science* **2016**, *353*, 150−154.
(19) Yin, H.; Chen, Z.; Peng, Y.; Xiong, S.; Li, Y.; Yamashita, H.; Li, J. Dual active centers bridged by oxygen vacancies of ruthenium single-atom hybrids supported on molybdenum oxide for photocatalytic ammonia synthesis. *Angew. Chem., Int. Ed.* **2022**, *61*, No. e202114242.
(20) Shi, L.; Xu, C.; Sun, X.; Zhang, H.; Liu, Z.; Qu, X.; Du, F. Facile fabrication of hierarchical $BiVO_4/TiO_2$ heterostructures for enhanced photocatalytic activities under visible-light irradiation. *J. Mater. Sci.* **2018**, *53*, 11329−11342.
(21) Yang, J.; Xie, T.; Liu, C.; Xu, L. Facile fabrication of dumbbell-like β-Bi_2O_3/graphene nanocomposites and their highly efficient photocatalytic activity. *Materials* **2018**, *11*, 1359.
(22) Zhang, X.; Valencia, A.; Li, W.; Ao, K.; Shi, J.; Yue, X.; Zhang, R.; Daoud, W. A. Decoupling activation and transport by electron-regulated atomic-Bi harnessed surface-to-pore interface for vanadium redox flow battery. *Adv. Mater.* **2024**, *36*, No. 2305415.
(23) Chen, K.; Ma, Z.; Li, X.; Kang, J.; Ma, D.; Chu, K. Single-atom Bi alloyed Pd metallene for nitrate electroreduction to ammonia. *Adv. Funct. Mater.* **2023**, *33*, No. 2209890.
(24) Leng, D.; Wang, T.; Du, C.; Pei, X.; Wan, Y.; Wang, J. Synthesis of β-Bi_2O_3 nanoparticles via the oxidation of Bi nanoparticles: Size, shape and polymorph control, anisotropic thermal expansion, and visible-light photocatalytic activity. *Ceram. Int.* **2022**, *48*, 18270−18277.
(25) Liu, B.; Zhang, B.; Liu, B.; Hu, Z.; Dai, W.; Zhang, J.; Feng, F.; Lan, B.; Zhang, T.; Huang, H. Surface hydroxyl and oxygen vacancies engineering in ZnSnAl LDH: Synergistic promotion of photocatalytic oxidation of aromatic VOCs. *Environ. Sci. Technol.* **2024**, *58*, 4404−4414.
(26) Chen, C.; Wu, M.; Xu, Y.; Ma, C.; Song, M.; Jiang, G. Efficient photoreduction of CO_2 to CO with 100% selectivity by slowing down electron transport. *J. Am. Chem. Soc.* **2024**, *146*, 9163−9171.
(27) Wang, D.; Luo, K.; Tian, H.; Cheng, H.; Giannakis, S.; Song, Y.; He, Z.; Wang, L.; Song, S.; Fang, J.; Ma, J. Transforming plain $LaMnO_3$ perovskite into a powerful ozonation catalyst: Elucidating the mechanisms of simultaneous A and B sites modulation for enhanced toluene degradation. *Environ. Sci. Technol.* **2024**, *58*, 12167−12178.
(28) Lu, Y.; Yang, Y.; Fan, X.; Li, Y.; Zhou, D.; Cai, B.; Wang, L.; Fan, K.; Zhang, K. Boosting charge transport in $BiVO_4$ photoanode for solar water oxidation. *Adv. Mater.* **2022**, *34*, No. 2108178.
(29) Hu, S.; Liu, X.; Wang, C.; Camargo, P. H. C.; Wang, J. Tuning thermal catalytic enhancement in doped MnO_2−Au nano-heterojunctions. *ACS Appl. Mater. Interface* **2019**, *11*, 17444−17451.
(30) Chen, C.; Wu, M.; Ma, C.; Song, M.; Jiang, G. Efficient photo-assisted thermal selective oxidation of toluene using N-doped TiO_2. *ACS Omega* **2023**, *8*, 21026−21031.
(31) Chen, C.; Wu, M.; Yang, C.; Yu, X.; Yu, J.; Yin, H.; Li, G.; Su, G.; Hao, Z.; Song, M.; Ma, C. Electron-donating N−−Ti3+−Ov interfacial sites with high selectivity for the oxidation of primary C-H bonds. *Cell Rep. Phys. Sci.* **2022**, *3*, No. 100936.
(32) Wang, J. W.; Zhao, F.; Velasco, L.; Sauvan, M.; Moonshiram, D.; Salati, M.; Luo, Z. M.; He, S.; Jin, T.; Mu, Y. F.; Ertem, M. Z.; Lian, T.; Llobet, A. Molecular catalyst coordinatively bonded to organic semiconductors for selective light-driven CO_2 reduction in water. *Nat. Commun.* **2024**, *15*, 9779.
(33) Kesavan, L.; Tiruvalam, R.; Rahim, M. H. A.; Saiman, M. I. B.; Enache, D. I.; Jenkins, R. L.; Dimitratos, N.; Lopez-Sanchez, J. A.; Taylor, S. H.; Knight, D. W.; Kiely, C. J.; Hutchings, G. J. Solvent-free oxidation of primary carbon-hydrogen bonds in toluene using Au-Pd alloy nanoparticles. *Science* **2011**, *331*, 195−199.
(34) Cao, X.; Chen, Z.; Lin, R.; Cheong, W. C.; Liu, S.; Zhang, J.; Peng, Q.; Chen, C.; Han, T.; Tong, X.; Wang, Y.; Shen, R.; Zhu, W.; Wang, D.; Li, Y. A photochromic composite with enhanced carrier separation for the photocatalytic activation of benzylic C-H bonds in toluene. *Nat. Catal.* **2018**, *1*, 704−710.
(35) Chen, C.; Wu, M.; Chen, B.; Ma, C.; Song, M.; Jiang, G. Triggering photocatalytic performance of $La_2Co_xMn_{2-x}O_6$ via heat activation. *Proc. Natl. Acad. Sci. U. S. A.* **2023**, *120*, No. e2310004120.

https://doi.org/10.1021/acscatal.5c03644
ACS Catal. 2025, 15, 15387−15394